View metadata, citation and similar papers at core.ac.uk

brought to you by CORE

provided by Haverford College: Haverford Scholarship

Haverford College

Haverford Scholarship

Faculty Publications

Astronomy

2000

Faint radio sources and star formation history

D. B. Haarsma

Bruce Partridge
Haverford College, bpartrid@haverford.edu

R. A. Windhorst

E. A. Richards

Follow this and additional works at: https://scholarship.haverford.edu/astronomy_facpubs

Repository Citation

(with D. B. Haarsma and others) Faint Radio Sources and Star Formation History, Ap. J., 544, 641, 2000.

This Journal Article is brought to you for free and open access by the Astronomy at Haverford Scholarship. It has been accepted for inclusion in Faculty Publications by an authorized administrator of Haverford Scholarship. For more information, please contact nmedeiro@haverford.edu.

Haverford College
Haverford Scholarship

Faculty Publications | Astronomy

2000

Faint radio sources and star formation history

D. B. Haarsma

R. Bruce Partridge
Haverford College

R. A. Windhorst

E. A. Richards

Follow this and additional works at: http://scholarship.haverford.edu/astronomy_facpubs

Repository Citation
(with D. B. Haarsma and others) Faint Radio Sources and Star Formation History, Ap. J., 544, 641, 2000.

This Journal Article is brought to you for free and open access by the Astronomy at Haverford Scholarship. It has been accepted for inclusion in Faculty Publications by an authorized administrator of Haverford Scholarship. For more information, please contact nmedeiro@haverford.edu.

THE ASTROPHYSICAL JOURNAL, 544:641–658, 2000 December 1
© 2000. The American Astronomical Society. All rights reserved. Printed in U.S.A.

FAINT RADIO SOURCES AND STAR FORMATION HISTORY

D. B. HAARSMA
Calvin College, 3201 Burton Street SE, Grand Rapids, MI 49546; dhaarsma@calvin.edu
R. B. PARTRIDGE
Haverford College, Haverford, PA 19041; bpartrid@haverford.edu
AND
R. A. WINDHORST AND E. A. RICHARDS[1]
Department of Physics and Astronomy, Arizona State University, Tempe, AZ 85287-1504; rogier.windhorst@asu.edu, eric.richards@asu.edu
Received 1999 November 26; accepted 2000 July 26

ABSTRACT

The centimeter-wave luminosity of local radio galaxies correlates well with their star formation rate. We extend this correlation to surveys of high-redshift radio sources to estimate the global star formation history. The star formation rate found from radio observations needs no correction for dust obscuration, unlike the values calculated from optical and ultraviolet data. Three deep radio surveys have provided catalogs of sources with nearly complete optical identifications and nearly 60% complete spectroscopic redshifts: the Hubble Deep Field and Flanking Fields at $12^h+62°$, the SSA13 field at $13^h+42°$, and the V15 field at $14^h+52°$. We use the redshift distribution of these radio sources to constrain the evolution of their luminosity function. The epoch-dependent luminosity function is then used to estimate the evolving global star formation density. At redshifts less than 1, our calculated star formation rates are significantly larger than even the dust-corrected optically selected star formation rates; however, we confirm the rapid rise from $z = 0$ to $z = 1$ seen in those surveys.

Subject headings: cosmology: observations — galaxies: evolution — galaxies: luminosity function, mass function — galaxies: starburst — radio continuum: galaxies — stars: formation

1. INTRODUCTION

In the last few years, a variety of observational methods have been used to study the global star formation history of the universe at a range of redshifts. Figure 1 compiles the results from several of these studies, scaling all to the same cosmology and initial mass function (IMF). In plotting the points, we used the corrections for extinction by dust calculated by Steidel et al. (1999, their Fig. 9). The diagram shows significant scatter in the star formation density at each redshift. Most studies agree, however, that the star formation density rises rapidly from $z = 0$ to $z = 1$. Beyond a redshift of 1 it is unclear whether the star formation density decreases significantly (as suggested at first by Madau et al. 1996) or stays roughly constant (e.g., Steidel et al. 1999).

Radio observations have important advantages in determining the global star formation history and are a useful complement to studies at other wavelengths. Unlike calculations based on ultraviolet and optical observations, there is no need to make uncertain corrections for dust extinction since the radio emission at $\nu \gtrsim 1$ GHz passes freely through dust. Compared to far-infrared and submillimeter studies, interferometric radio observations typically have better positional accuracy, allowing for more reliable identifications with objects detected at other wavelengths (Richards 1999; Downes et al. 1999). Finally, since far-infrared emission is due to reheated dust, the original source of energy (whether star formation or active galactic nuclei [AGNs]) can be unclear; radio properties, such as spectral index and morphology, can help distinguish between these. We do note, however, that contamination of the radio flux by emission from AGNs is a problem (addressed in § 2.5). In addition, relatively few high-redshift star-forming radio sources have as yet been detected (though current and planned deep radio surveys will rapidly change that). As a consequence, the statistical sample used in this work is small.

Our strategy in this paper is as follows. We use very sensitive radio surveys to detect star-forming galaxies at high redshift. Not all of the sources in these surveys are star-forming (some are probably AGNs), but we deal with this problem by defining data samples that give lower and upper limits to the star formation history, as described in § 2. Next, in § 3 we use these data to determine the evolving luminosity function for star-forming radio sources. The redshift and flux distribution of the sources, as well as the total extragalactic radio background, are used to constrain the evolution. In § 4 we use the well-known relationship between radio luminosity and star formation rate (and discuss the assumption that this relationship holds for all redshifts) to find the star formation history directly from the observed radio sources. The evolving luminosity function is used to correct for faint sources below the observational detection limits. We discuss our conclusions in § 5.

Unless stated otherwise, we assume a cosmology of $H_0 = 50$, $\Omega_m = 1$, and $\Omega_\Lambda = 0$ and a nonevolving Salpeter IMF with a stellar mass range of 0.1–100 $M_\odot$. We use a radio spectral index of $\alpha = 0.4$ (where $S \propto \nu^{-\alpha}$), which is appropriate for faint sources selected at 5 or 8 GHz (Windhorst et al. 1993; Richards 2000).

2. THE DATA SETS

2.1. *Surveys*

Three fields have been observed to microjansky sensitivities at centimeter wavelengths and also have extensive

[1] Hubble Fellow.

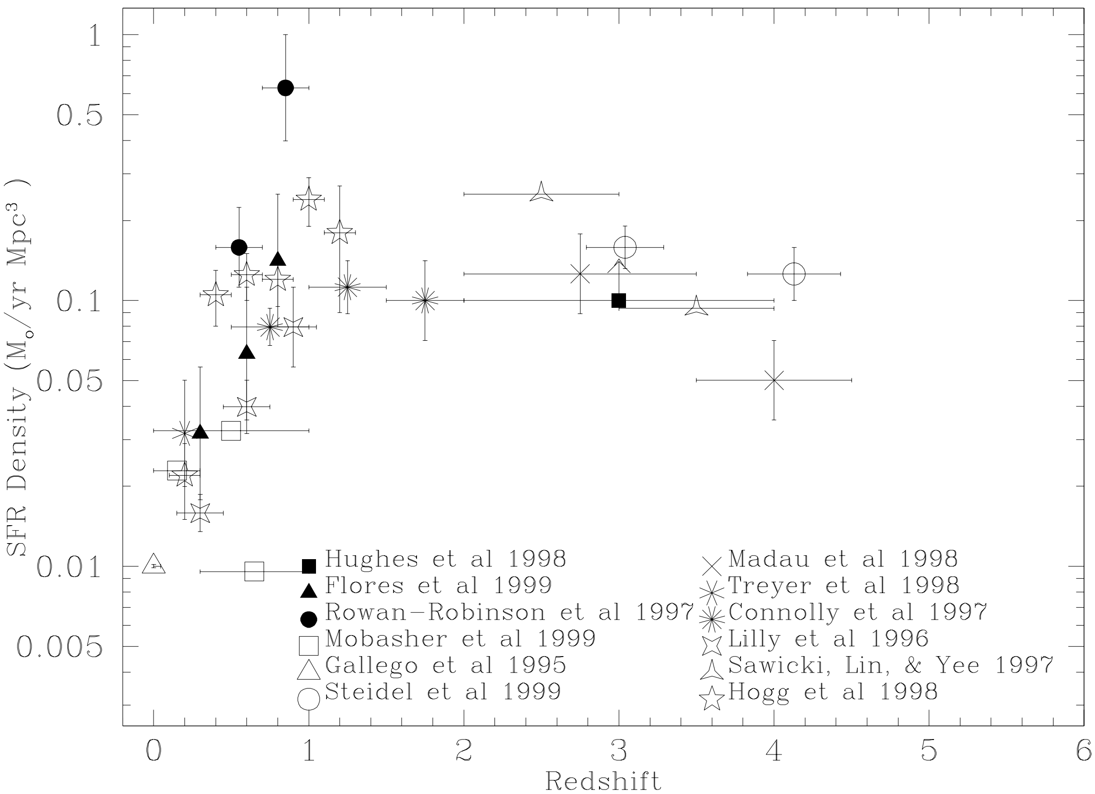

FIG. 1.—Some star formation histories at various wavelengths (Hughes et al. 1998; Flores et al. 1999; Rowan-Robinson et al. 1997; Mobasher et al. 1999; Gallego et al. 1995; Steidel et al. 1999; Madau et al. 1998; Treyer et al. 1998; Connolly et al. 1997; Lilly et al. 1996; Sawicki, Lin, & Yee 1997; Hogg et al. 1998). All the data points are scaled to $H_0 = 50$, $\Omega_m = 1$, $\Omega_\Lambda = 0$, and a Salpeter IMF from 0.1 to 100 $M_\odot$ (following the scaling by Baugh et al. 1998, their Fig. 16). Corrections for dust extinction calculated by Steidel et al. (1999, their Fig. 9) were used.

photometric and spectroscopic data: the Hubble Deep Field (HDF) at 8 GHz, the SSA13 field at 8 GHz, and the V15 field at 5 GHz. Table 1 summarizes information on the three fields, all of which were observed at the Very Large Array[2] (VLA). Tables 2, 3, and 4 list the individual sources in each field; the columns are as follows.

Column (*1*).—The source name.

[2] The National Radio Astronomy Observatory is a facility of the National Science Foundation operated under cooperative agreement by Associated Universities, Inc.

Columns (*2*) *and* (*3*).—S_8, S_5, and $S_{1.4}$ are the radio flux densities at 8, 5, and 1.4 GHz, respectively. If a measured value of $S_{1.4}$ is not available, we use the spectral index shown in column (4) to calculate $S_{1.4}$ and list the value in parentheses in column (3).

Column (*4*).—The radio spectral index, α, defined as $S \propto \nu^{-\alpha}$. If 1.4 GHz measurements are not available, we assume a spectral index of 0.4 unless this violates the survey detection threshold at 1.4 GHz.

Column (*5*).—The primary beam correction factor, B_i (see § 2.2, eq. [1]).

TABLE 1

SUMMARY OF RADIO SURVEYS

Field	Band (GHz)	Flux Limit at Field Center (μJy)	Field Size (arcmin^2)	N	N_{sp}	N_{ph}	N_a
Hubble Deep Field[a] ($12^h+62°$)......	8	9	66	29	19	4	6
SSA13 field[b] ($13^h+42°$)	8	8.8	7	15	8	3	4
V15 field[c] ($14^h+52°$)..................	5	16	86	33	18	3	12
Total	...	...	...	77	45	10	22

NOTE.—The listed flux limit for each field is approximately 5 times the rms noise at the beam center. The field size is the region in which both radio and optical data are available (see Tables 2–4 for details). N is the total number of sources above the flux limit, N_{sp} is the number of those sources with spectroscopic redshifts, N_{ph} is the number with redshifts estimated from I- or HK'-band magnitudes, and N_a is the number with redshifts randomly assigned (see § 2.3 for how assignments were made).

[a] Richards et al. 1998.

[b] Windhorst et al. 1995.

[c] Fomalont et al. 1991; Hammer et al. 1995.

TABLE 2

HDF

Name (1)	S_8 (μJy) (2)	$S_{1.4}$ (μJy) (3)	α (4)	B_i (1 arcsec^{-2}) (5)	Galaxy Type (6)	Redshift Type (7)	z (8)	HK' (mag) (9)	I (mag) (10)	z_{max} (11)	log ($L_{e,1.4}$) [log (W/Hz)] (12)	SFR ($M_\odot$ yr^{-1}) (13)	Sample (14)
3632+1105......	21.8	(23)	<0.03	0.037	sim	sp[a]	0.518	17.22	19.79	0.785	22.49	37	U, M, L
3634+1212......	56.5	211	0.74	0.019	sim	sp[a, b]	0.458	16.38	19.10	0.966	23.45	340	U, M, L
3634+1240......	52.6	198	0.74	0.020	sim	sp[b, c]	1.219	19.11	22.29	2.34	24.49	3700	U, M, L
3637+1135......	17.5	(23)	<0.15	0.049	sim	sp[c]	0.078	17.07	18.61	0.108	20.78	1	U, M, L
3640+1010......	29.2	65	0.45	0.029	fr	afr	1.1	21.22	>25	1.78	23.80	750	U
3641+1142......	18.6	30	0.27	0.045	sim	sp[a]	0.548	19.26	22.07	0.759	22.70	61	U, M, L
3642+1331......	79.9	432	0.94	0.016	el	sp[d]	4.42	21.23	>25	9.12	26.52	...	U
3642+1545......	53.6	131	0.50	0.020	un (sim)	sp[a, b]	0.857	18.07	20.86	1.76	23.85	860	U, M
3644+1133......	752	1290	0.30	0.015	el	sp[b, c]	1.050	17.64	21.04	6.38	25.00	...	U
3644+1249......	10.2	(21)	(0.4)	0.249	sim	sp[c]	0.557	18.30	20.59	0.589	22.59	47	U, M, L
3646+1404......	190	177	−0.04	0.015	sim	sp[b, c, e]	0.962	18.19	20.75	3.85	23.95	1100	U, M, L
3646+1447......	13.3	77	0.98	0.081	el	ph	0.69	20.21	22.05	0.804	23.50	<390	U
3646+1448......	24.7	112	0.84	0.033	fr	afr	1.5	>22	>25	2.16	24.52	4000	U
3649+1313......	14.0	51	0.72	0.072	sim	sp[b, c]	0.475	18.68	21.10	0.575	22.87	90	U, M, L
3651+1030......	26.0	99	0.74	0.031	sim	sp[b, c, e]	0.410	17.37	19.89	0.638	23.01	120	U, M, L
3651+1221......	16.8	60	0.71	0.052	fr	afr	1.7	>21.5	>25	2.16	24.34	2700	U
3652+1444......	185	148	−0.12	0.015	el	sp[b, c, e]	0.322	16.53	18.70	1.35	22.84	<83	U
3653+1139......	15.1	60	0.77	0.062	sim	sp[a, b]	1.275	19.44	21.90	1.55	24.04	1300	U, M, L
3655+1311......	12.3	(23)	<0.35	0.102	el	sp[a]	0.968	18.62	21.62	1.11	23.18	<180	U
3657+1455......	15.3	(23)	<0.23	0.061	un (sim)	sp[a]	0.859	18.83	21.44	1.07	23.01	120	U, M
3700+0908......	66.7	326	0.89	0.018	fr	afr	2.9	20.98	>25	5.75	25.82	...	U
3701+1146......	29.5	98	0.67	0.028	fr	sp[a, b]	0.884	20.14	24.81	1.41	23.80	770	U, M
3707+1408......	29.0	49	0.29	0.029	fr	ph	2.07	20.29	24.70	3.35	24.28	2300	U, M
3708+1056......	26.4	49	0.35	0.031	sim	sp[a, b]	0.423	17.91	19.87	0.684	22.68	57	U, M, L
3708+1246......	19.5	(23)	<0.09	0.042	sim	ph	0.887	19.82	21.73	1.24	23.01	120	U, M
3711+1331......	31.1	108	0.69	0.027	sim	ph	1.53	19.59	22.75	2.42	24.47	3600	U, M
3716+1512......	85.8	180	0.41	0.016	sim	sp[b]	0.558	17.36	19.80	1.45	23.53	410	U, M, L
3721+1129......	630	383	−0.28	0.015	fr	afr	2.5	20.90	>25	>10	25.07	...	U
3725+1128......	530	5960	1.35	0.015	fr	afr	2.7	>21.5	>25	9.12	27.25	...	U

Note.—These sources are cataloged by Richards et al. 1998, who give the detailed source positions. Sources are included here only if they are within 4′.6 of the radio field center and above the 8 GHz radio flux limit of Richards et al. 1998 (additional sources were detected in Richards 2000 but are not included because of their complicated primary beam corrections and lack of spectroscopic redshifts). The flux measurements, S_8 and $S_{1.4}$, are from Richards 2000. Several sources were identified as faint/red by Richards et al. 1999. The I and HK' magnitudes are from Barger et al. 1999. The remaining quantities in the table are calculated or assigned in this work.

[a] Cohen et al. 2000.
[b] Barger et al. 2000.
[c] Cohen et al. 1996.
[d] Waddington et al. 1999.
[e] Lowenthal et al. 1997.

TABLE 3

SSA13

Name (1)	S_8 (μJy) (2)	$S_{1.4}$ (μJy) (3)	α (4)	B_i (1 arcsec^{-2}) (5)	Galaxy Type (6)	Redshift Type (7)	z (8)	HK' (mag) (9)	I (mag) (10)	$z_{\max}$ (11)	log ($L_{e,1.4}$) [log (W/Hz)] (12)	SFR ($M_\odot$ yr^{-1}) (13)	Sample (14)
(1) 1214+3822	8.9	(18)	(0.4)	0.245	fr	afr	1.5	21.95	>25	1.51	23.56	440	U
(3) 1215+3703	14.1	(29)	(0.4)	0.141	un (sim)	sp	0.322	18.70	20.81	0.398	22.19	19	U, M
(5) 1216+3921	33.7	(69)	(0.4)	0.141	fr	afr	2.3	>25	>25	3.94	24.60	4800	U
(6) 1217+3913	24.1	(49)	(0.4)	0.141	un (sim)	sp	0.494	17.57	19.99	0.767	22.84	84	U, M
(7) 1218+3931	15.1	(31)	(0.4)	0.141	fr	ph	2.54	21.22	>25	3.16	24.36	2800	U, M
(9) 1218+3844	26.6	(45)	(0.4)	0.141	un (el)	sp	0.698	17.57	20.62	1.12	23.23	<210	U
(10) 1220+3833......	18.3	(37)	(0.4)	0.141	un (sim)	a	0.559	21.78	24.08	0.767	22.85	85	U
(11) 1220+3703......	14.3	(29)	(0.4)	0.141	fr	ph	2.02	20.77	>25	2.45	24.08	1500	U, M
(12) 1220+3923......	14.3	(29)	(0.4)	0.141	fr	afr	1.9	23.36	>25	2.32	24.02	1300	U
(13) 1221+3923......	10.1	(21)	(0.4)	0.225	sim	sp	0.302	17.08	19.42	0.323	21.99	12	U, M, L
(15) 1221+3723......	18.3	(37)	(0.4)	0.141	sim	sp	0.180	17.04	18.99	0.254	21.76	7	U, M, L
(16) 1222+3827......	17.4	(36)	(0.4)	0.141	un (sim)	ph	0.685	19.38	22.03	0.923	23.03	130	U, M
(18) 1223+3909......	21.1	(43)	(0.4)	0.141	un (el)	sp	0.765	17.19	19.92	1.11	23.23	<200	U
(19) 1224+3712......	29.2	(60)	(0.4)	0.141	un (sim)	sp	0.401	16.68	19.14	0.684	22.72	63	U, M
(24) 1228+3800......	23.8	(49)	(0.4)	0.141	sim	sp	0.316	17.04	19.60	0.495	22.40	30	U, M, L

NOTE.—These sources are cataloged by Windhorst et al. 1995 (catalog number in parentheses), who give the detailed source positions; the source name is derived from its radio position. Sources are included here if they are above the radio flux limit of K. I. Kellermann et al. 2000, in preparation, fully within the optical field of Windhorst et al. 1995, and not identified with quasars or stars. The I and HK' magnitudes are from Cowie et al. 1996. The S_8 flux densities are from K. I. Kellermann et al. 2000, in preparation. Sources 1, 5, 7, 11, and 12 are classified as faint/red by Richards et al. 1999. The spectroscopic redshifts for sources 3, 13, 15, and 19 are from Windhorst et al. 1994a, and those for sources 6, 9, 18, and 24 are from J. Lowenthal (2000, private communication). The remaining quantities in the table are calculated or assigned in this work.

TABLE 4

V15

Name (1)	S_5 (μJy) (2)	$S_{1.4}$ (μJy) (3)	α (4)	B_i (1 arcsec^{-2}) (5)	Galaxy Type (6)	Redshift Type (7)	z (8)	HK′ (mag) (9)	I (mag) (10)	z_{max} (11)	log ($L_{e,1.4}$) [log (W/Hz)] (12)	SFR ($M_\odot$ yr^{-1}) (13)	Sample (14)
15V 05	41	96	0.68	0.019	sim	sp	0.989	...	22.04	1.42	23.92	1000	U, M, L
15V 10	1912	2560	0.23	0.012	el	a	0.180	20.86	22.27	1.53	23.58	<460	U
15V 11	70	171	0.71	0.014	sim	sp	0.375	...	19.86	0.700	23.16	170	U, M, L
15V 15	24	(40)	(0.4)	0.034	el	a	0.302	...	22.30	0.363	22.27	<22	U
15V 18	44	(73)	(0.4)	0.018	fr	ph	2.0	21.1	>25	2.99	24.47	3600	U, M
15V 19	24	(43)	(0.4)	0.034	sim	sp	0.754	...	21.17	0.902	23.17	180	U, M, L
15V 21	298	807	0.80	0.012	sim	sp	0.724	...	21.29	2.19	24.53	4100	U, M, L
15V 23	54	(80)	<0.31	0.016	el*	sp	1.149	...	21.08	1.91	23.89	930	U
15V 24	79	141	0.46	0.014	sim	sp	0.660	19.22	20.64	1.29	23.60	480	U, M, L
15V 26a	23	(38)	(0.4)	0.037	el*	sp	0.372	...	21.87	0.442	22.45	<34	U
15V 26b	24	(40)	(0.4)	0.034	el*	sp	0.155	...	19.27	0.188	21.64	<5	U
15V 28	74	(80)	<0.6	0.014	el	sp	0.988	19.99	21.74	1.95	23.66	<550	U
15V 33	20	(33)	(0.4)	0.054	el	a	0.410	...	23.2	0.457	22.49	<37	U
15V 34	1311	1160	−0.10	0.012	el	sp	0.838	...	22.01	6.46	24.62	...	U
15V 37	51	(80)	<0.36	0.016	el	ph	2.52	20.53	23.65	4.03	24.74	...	U
15V 39	35	(58)	(0.4)	0.021	el	sp	0.992	19.89	21.85	1.38	23.62	<500	U
15V 40	33	106	0.93	0.022	el	sp	0.976	19.67	21.94	1.29	24.02	<1300	U
15V 45	33	150	1.21	0.022	el	a	0.475	...	24.3	0.631	23.42	<320	U
15V 47	53	131	0.72	0.016	sim	sp	0.809	22.23	23.00	1.30	23.85	850	U, M, L
15V 48	20	(33)	(0.4)	0.054	sim	sp	0.743	...	21.11	0.822	23.08	150	U, M, L
15V 49	31	96	0.90	0.023	un (sim)	ph	0.537	19.22	19.96	0.700	23.31	180	U, M
15V 50	705	1722	0.71	0.012	un (el)	a	0.654	...	22.76	2.79	24.74	...	U
15V 51	41	(68)	(0.4)	0.019	un (sim)	a	0.724	...	23.14	1.08	23.36	280	U
15V 53	30	85	0.83	0.024	sim	a	0.754	...	23.04	0.966	23.61	490	U
15V 57	37	(61)	(0.4)	0.020	el*	sp	0.010	17.83	17.70	0.0153	19.40	<1	U
15V 59	19	(31)	(0.4)	0.066	un (sim)	a	0.960	...	24.5	1.04	23.32	250	U
15V 60	39	(64)	(0.4)	0.019	sim	sp	0.812	...	21.94	1.19	23.46	350	U, M, L
15V 62	24	(40)	(0.4)	0.034	fr	afr	2.1	>21.3	>25	2.48	24.26	2200	U
15V 67	46	(76)	(0.4)	0.017	fr	afr	2.5	...	>25	3.80	24.73	...	U
15V 70	576	2414	1.14	0.012	fr	afr	1.3	...	>25	4.27	25.80	...	U
15V 72	46	(76)	(0.4)	0.017	el	a	1.219	20.9	23.8	1.88	23.96	1100	U
15V 73	37	(61)	(0.4)	0.020	el	sp	0.746	...	20.95	1.07	23.35	<270	U
15V 81	28	(46)	(0.4)	0.026	el*	sp	1.158	...	22.16	1.46	23.69	<590	U

NOTE.—These sources are cataloged by Fomalont et al. 1991, who give detailed source positions and the 5 and 1.4 GHz flux densities. Sources are not included here if they are quasars, stars, below the radio flux limit, or outside the optical field of Hammer et al. 1995. Sources 30, 36, 41, and 69 were found later to be pairs of radio sources, with both members of the pair below the radio flux limit, and so are not included. The galaxy types, spectroscopic redshifts, and *I* and *K* magnitudes are from Hammer et al. 1995. An asterisk (*) indicates that Hammer et al. 1995 classified the galaxy type based on its emission lines, which they find to be more characteristic of AGNs than starbursts. The spectroscopic redshifts for 15V 5 and 15V 47 and the galaxy type for 15V 47 are from Brinchmann et al. 1998. Lilly et al. 1999 find a photometric redshift of 2 for 15V 18. Flores et al. 1999 identify source 23 as a Seyfert 2 galaxy. The remaining quantities in the table are calculated or assigned in this work.

Column (*6*).—The galaxy type (see § 2.4): "sim" refers to spiral, irregular, or merger; "el" refers to elliptical; "fr" refers to faint ($I > 25$) or red ($I - K > 4$); and "un" refers to unknown type or undetected. The galaxy type in parentheses is the assumed galaxy type in the case of "un."

Column (*7*).—The redshift type (see § 2.3): "sp" refers to spectroscopic, "ph" refers to rough photometric (based on I or HK' magnitudes), "a" refers to random assignment, and "afr" refers to random assignments for galaxies of type faint/red.

Column (*8*).—The redshift used in calculations.

Columns (*9*) *and* (*10*).—The I and HK' magnitudes. K magnitudes are converted to HK' magnitudes by $K = HK' - 0.3$.

Column (*11*).—The maximum redshift, $z_{\rm max}$, at which the galaxy would have been detected, based on its emitted luminosity $L_{e,1.4}$.

Column (*12*).—The log of the luminosity emitted at 1.4 GHz.

Column (*13*).—The star formation rate for each individual galaxy, derived from its radio luminosity ($L_{e,1.4}$) and equation (15). If the source is elliptical (or assumed elliptical), the emission is probably contaminated by AGNs and the calculated star formation rate is only an upper limit. For some of these sources, the AGN contamination causes the calculated star formation rate to be unphysically large (>5000 $M_{\odot}$ yr^{-1}), so it does not provide an interesting upper limit and we do not list it; we do, however, include these sources in our "upper" sample to give conservative upper limits on our results.

Column (*14*).—The samples to which the source was assigned (see § 2.5); "U" refers to the upper sample, "M" to the middle sample, and "L" to the lower sample.

For the first time we have a sample of microjansky radio sources with nearly complete optical identifications and nearly 60% complete spectroscopic redshift measurements. Others are doing similar work on faint star-forming radio galaxies (Hopkins et al. 1999; Mobasher et al. 1999; Benn et al. 1993; Gruppioni, Mignoli, & Zamorani 1999) with larger catalogs of sources. While our survey samples have fewer sources, we have generally more sensitive radio flux limits and more complete optical follow-up. In principle, this allows us to probe higher redshifts and to increase the fraction of sources identified with star-forming galaxies (see § 2.4).

2.2. *Primary Beam Corrections*

In each of the three radio surveys, the flux threshold varies significantly across the field as a result of the shape of the primary beam response of the VLA antennas. The flux limit listed in Table 1 is for the center of the field; the limiting flux $S_{\rm lim}$ increases to the edge of the field by about 1.5 for SSA13 and by about 10 for the larger HDF and V15 fields. To find the total surface density of sources n (the number of sources per angular area on the sky), we determine the contribution of each source by considering the portion of the field in which that source could have been detected. Therefore, each source i contributes

$$B_i = \frac{1}{A_i(S_i, S_{\rm lim})} \quad (1)$$

to the surface density of sources, where A_i is the solid angle on the sky in which the flux S_i of source i would be greater than the sensitivity limit of the radio survey $S_{\rm lim}$. A faint source that could only be detected at the center of the field (small A_i) contributes more to the average surface density n than a strong source that could be detected over the entire primary beam area (large A_i). To determine A_i for each source, we used the shape of the VLA primary beam.[3] The total surface density of sources for a survey is then

$$n = \Sigma B_i \, . \quad (2)$$

Other instrumental effects that affect the point source sensitivity across the field, such as bandwidth smearing, time delay smearing, and geometrical smearing (Richards 2000), are negligible in the three VLA surveys. Pascarelle, Lanzetta, & Fernández-Soto (1998) discuss the importance of surface brightness corrections in determining star formation history. However, the relatively low resolution of these radio surveys (3″ for the HDF and 3″–10″ for the SSA13 and V15 fields), combined with the resolution correction as a function of flux density (Windhorst et al. 1993), suggests that few of these sources are resolved and thus no correction for surface brightness biases has been made.

2.3. *Redshifts*

The redshifts for the sources in the sample are either spectroscopic measurements, estimates from I- or HK'-band magnitudes, or random assignments (see Tables 1–4). About 58% of the sources have spectroscopic redshifts. The highest spectroscopic redshift in the sample is a source at $z = 4.42$ in the HDF (Waddington et al. 1999); however, there is some evidence that this source may contain an AGN, so that its radio flux is not dominated by star formation (see § 2.5 for how this source is treated in the calculations).

For 13% of the sources, approximate redshifts were found from I- and HK'-band magnitudes. Windhorst et al. (1994b) used Bruzual-Charlot (1993) models to find the dependence of I and HK' magnitude on redshift for millijansky radio sources; these models are plotted in Figure 2. When comparing these models with the 45 spectroscopic redshifts in our sample of fainter microjansky radio sources, we found a significant dependence on radio flux density. We compensated by shifting the magnitude scale of these models to fit the I or HK' values of our sources that *do* have spectroscopic redshifts, with different shifts for different radio flux ranges (as listed in the caption of Fig. 2). We then used the revised curves to estimate redshifts for our sources that have I- or HK'-band magnitudes but not spectroscopic redshifts. The resulting redshifts are crude but are better than random assignments. We converted K magnitudes to HK' using $K = HK' - 0.3$ (Barger et al. 1999). The $I(z)$ model is double valued for $z \gtrsim 1$, and the $HK(z)$ model increases sharply for $z \gtrsim 3$, so when the I or HK' magnitude of a source indicated a redshift above these limits, we randomly assigned a redshift instead (see below).

For the remaining 29% of the sources, neither spectroscopic redshifts nor rough photometric redshifts were available. Rather than removing these sources from the sample, we assigned redshifts in the following manner. We first separated the sources into two groups: those with very faint

[3] The gain of the VLA primary beam is well matched by $g(r) = \{\cos[(-0.23226 + 74.567639rv)/57.2957795]\}^6$, where r is the distance from the beam center in degrees and v is the observing frequency in GHz (Oort & Windhorst 1985).

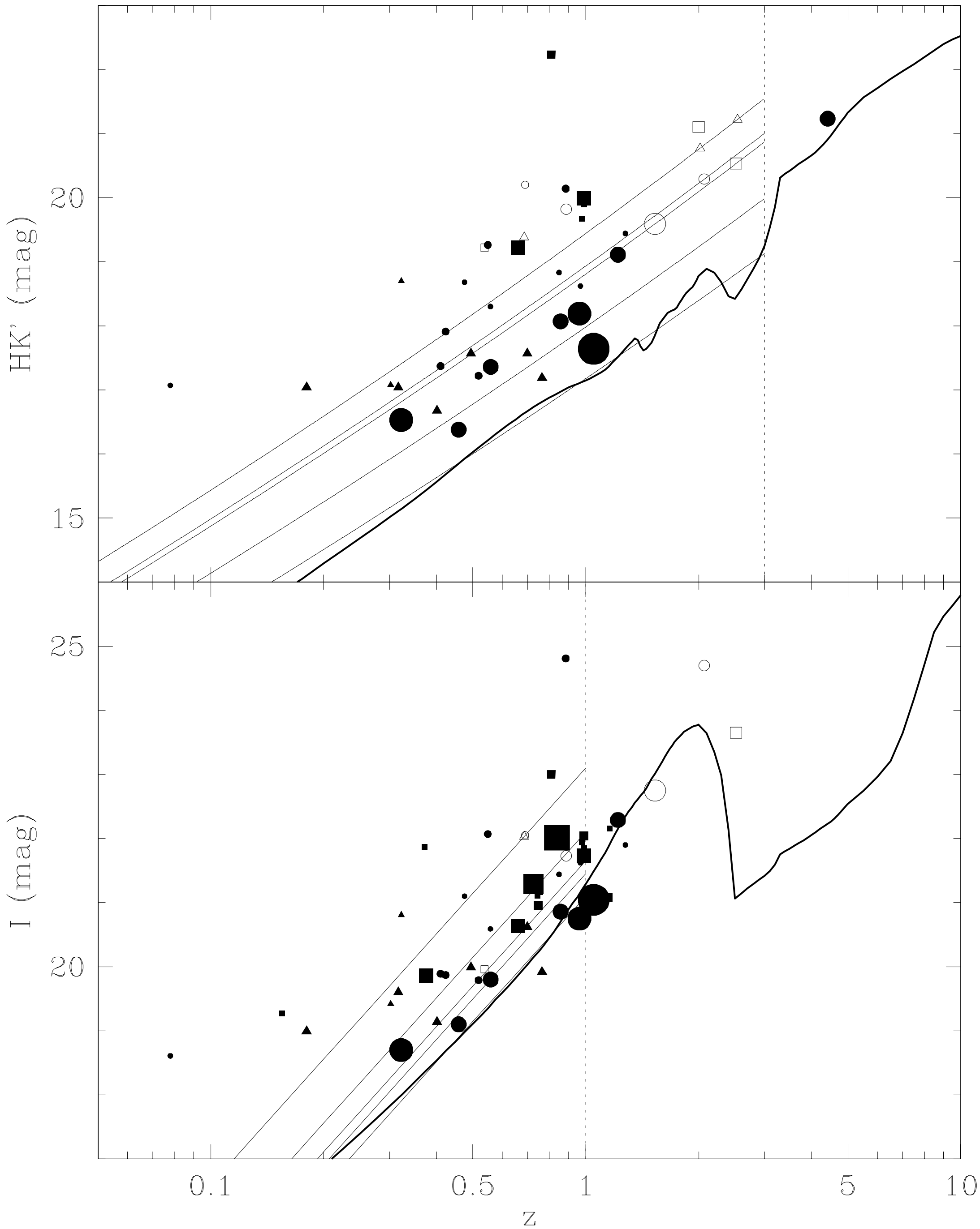

FIG. 2.—Estimation of photometric redshifts (see § 2.3). Circles are sources in the HDF field, triangles in the SSA13 field, and squares in the V15 field. The symbol size is proportional to radio flux density. Solid symbols are spectroscopic redshifts, hollow symbols are photometric redshifts. The thick line is the model for the $I(z)$ and $HK'(z)$ relationships for faint radio sources (Windhorst et al. 1994b). The thin lines are parallel to the model curve but are offset vertically to fit the spectroscopic redshifts in different radio flux density ranges. From bottom to top these flux ranges are $S_8 > 300$ μJy, $300 > S_8 > 100$ μJy, $100 > S_8 > 30$ μJy, $30 > S_8 > 18$ μJy, and $S_8 < 18$ μJy.

($I > 25$) or red ($I - K > 4$) optical identifications and those with brighter optical identifications. The sources in the group with brighter identifications (10 sources) were assigned redshifts randomly selected from the list of spectroscopic redshifts of star-forming galaxies in the sample. The sources in the group with very faint or red optical identifications (12 sources) are probably star-forming galaxies at redshifts greater than 1 (Richards et al. 1999; Barger, Cowie, & Richards 2000). These sources were assigned redshifts randomly in the range $z = 1$–3.

The redshift distributions and total source densities of the three surveys are strikingly different (see Fig. 3). The HDF and SSA13 surveys were both performed at 8 GHz with similar flux limits, yet the average source density (including all redshifts) is 1.3 sources arcmin^{-2} in the HDF, but 2.7 sources arcmin^{-2} in the SSA13 field, over twice as great. The total source density of the V15 field at 5 GHz is 0.7 sources arcmin^{-2}, which is nearly the same as the HDF field when the differences in flux limit and observing frequency are taken into account. The redshift distribution in

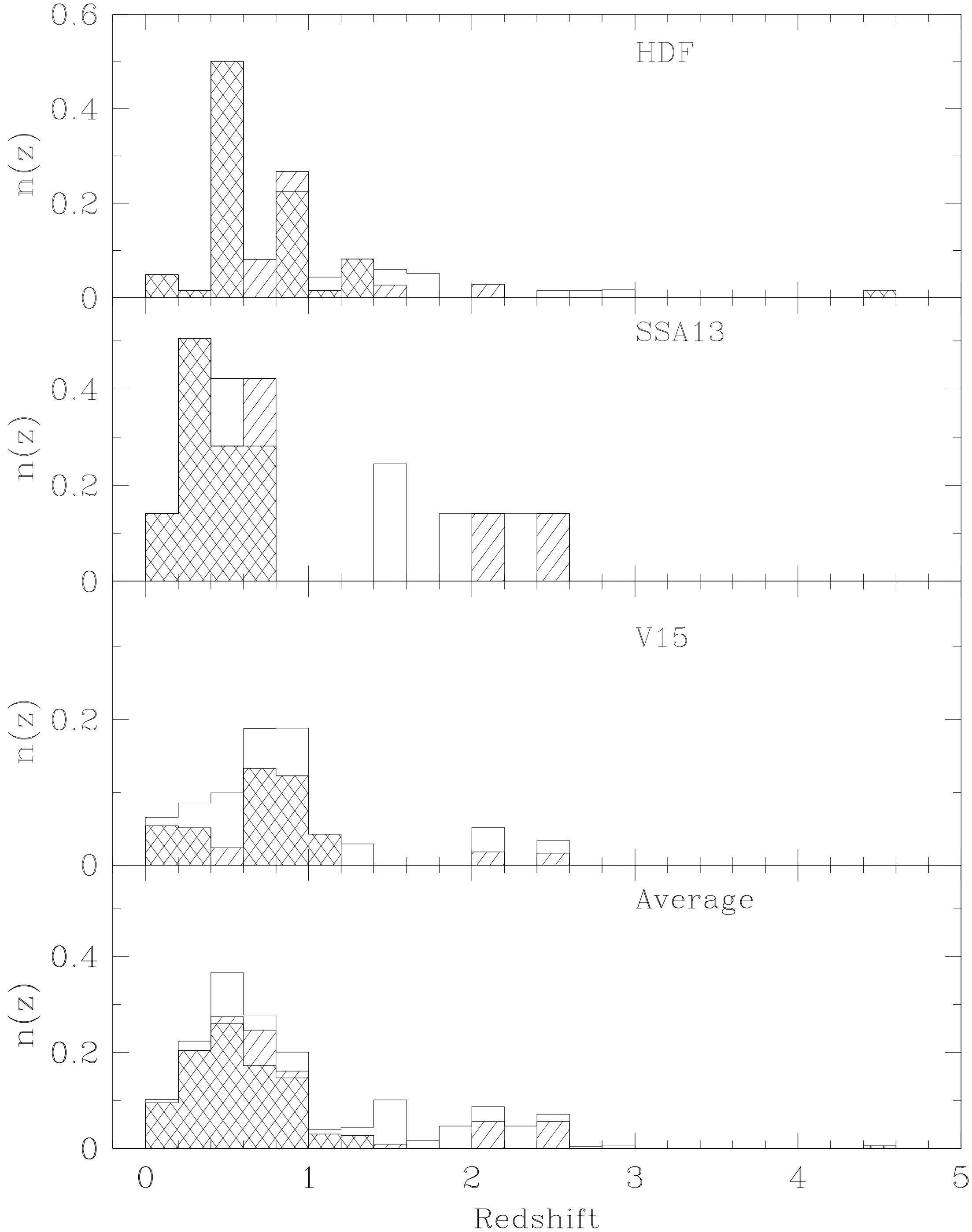

FIG. 3.—Redshift distribution of sources, in number arcmin^{-2} and corrected for the primary beam (§ 2.2). Redshifts were measured spectroscopically (*cross-hash*), estimated from *I*- or *HK*′-band magnitudes (*hash*), or assigned (*blank*; see § 2.3 for how assignments were made).

the three fields peaks at somewhat different redshifts (see Fig. 3), possibly as a result of galaxy superclustering or other high-redshift structure, although all three fields peak at $z < 1$ and have a long tail that extends to $z \sim 3$. The differences in the redshift distribution of the fields are probably due to cosmic variance (note that each field is sampling only a small solid angle). Since these fields were generally chosen to be free of bright sources, the number counts may be too low in the HDF and V15 fields rather than too high in the SSA13 field (indeed, Richards 2000 reports a deficit of radio sources detected at 1.4 GHz in the HDF). To deal with the differences between fields, we average the three data sets together in our calculations.

2.4. *Optical Identifications*

Figure 4 indicates the nature of the available optical identifications of the radio sources. Known quasi-stellar objects (QSOs) were removed from the sample (two from the SSA13 field, one from V15), as was one star in the V15 field, and are not shown in the figure. For the remaining sources, the three fields appear to be significantly different. In the HDF,

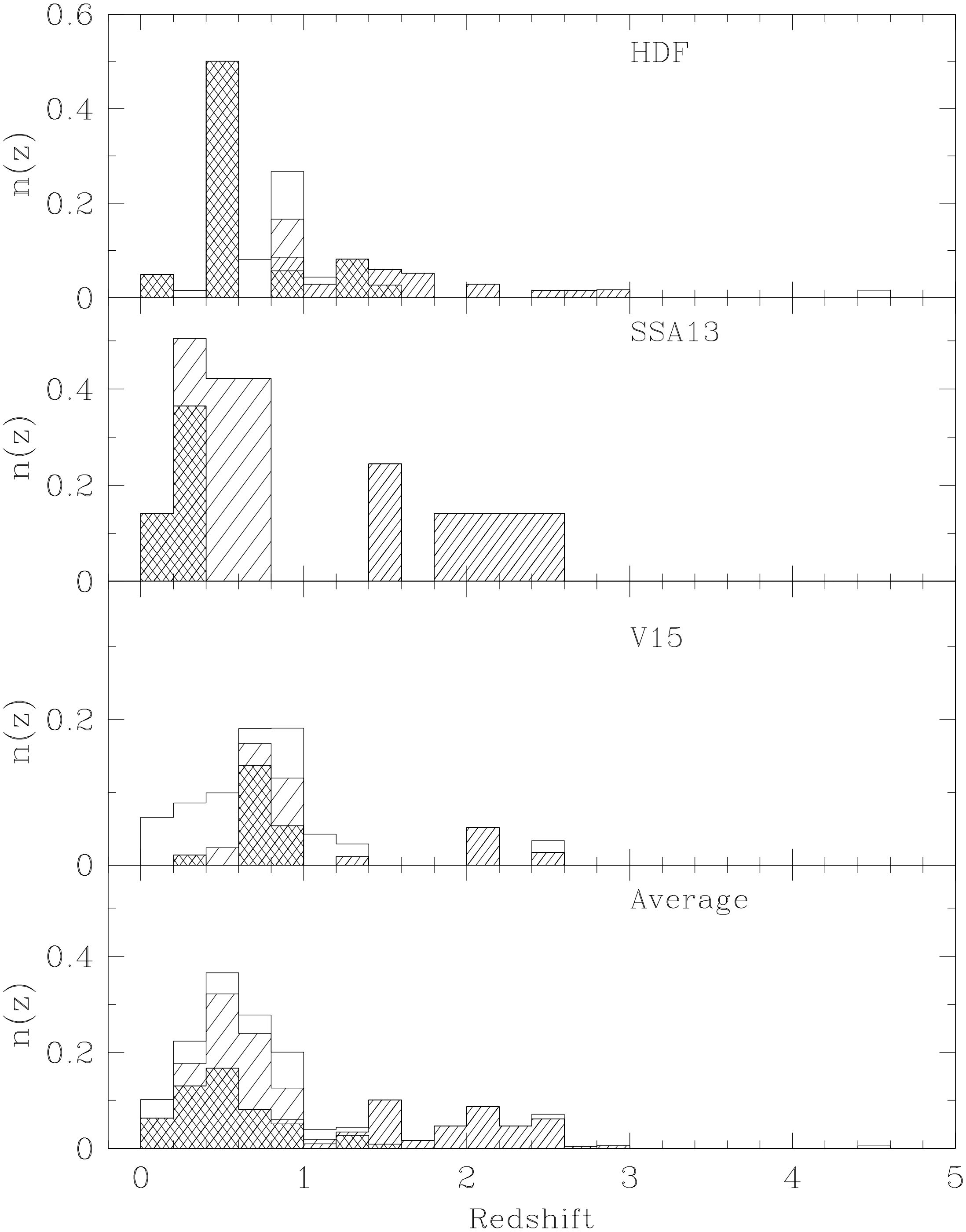

FIG. 4.—Redshift distribution of sources, separated by galaxy type, in number arcmin^{-2} and corrected for the primary beam shape (§ 2.2). Indicated are spiral, irregular, or merging galaxies (*cross-hash*), very faint or red optical identifications (*narrow hash*), unknown or unclear identifications (*broad hash*), and elliptical or emission-line galaxies (*blank*). Known QSOs and stars (just four sources in the three surveys) are not included in the figures or our calculations.

about 50% of the radio sources have star-forming counterparts (spirals, mergers, and irregulars; Richards et al. 1998); another 30% are in the red/optically faint category discussed above (several of which are identified with bright submillimeter objects and may include star-forming galaxies; Barger et al. 2000); and only 20% are identified with elliptical galaxies that presumably are associated with low-luminosity AGNs. In the SSA13 field, 50% are identified with star-forming or red/optically faint galaxies, and 50% are of unknown type. In the V15 field, 15% of the sources have unknown galaxy types, and 40% of the sources are likely to be star-forming or in the red/optically faint population (Hammer et al. 1995). A further 35% are claimed to be elliptical/AGN counterparts based on deep *I*-band images from the Canada-France Hawaii Telescope, and another 15% are classified by Hammer et al. (1995) as AGNs based on emission-line studies. Thus, Hammer et al. (1995) report a larger fraction of low-luminosity AGNs in the V15 field (50%) than observed in the HDF (20%). However, HST/WFPC2 images of these identifications from the Groth Strip survey (Hammer 1996) show some ambiguity in the optical identifications, indicating a higher

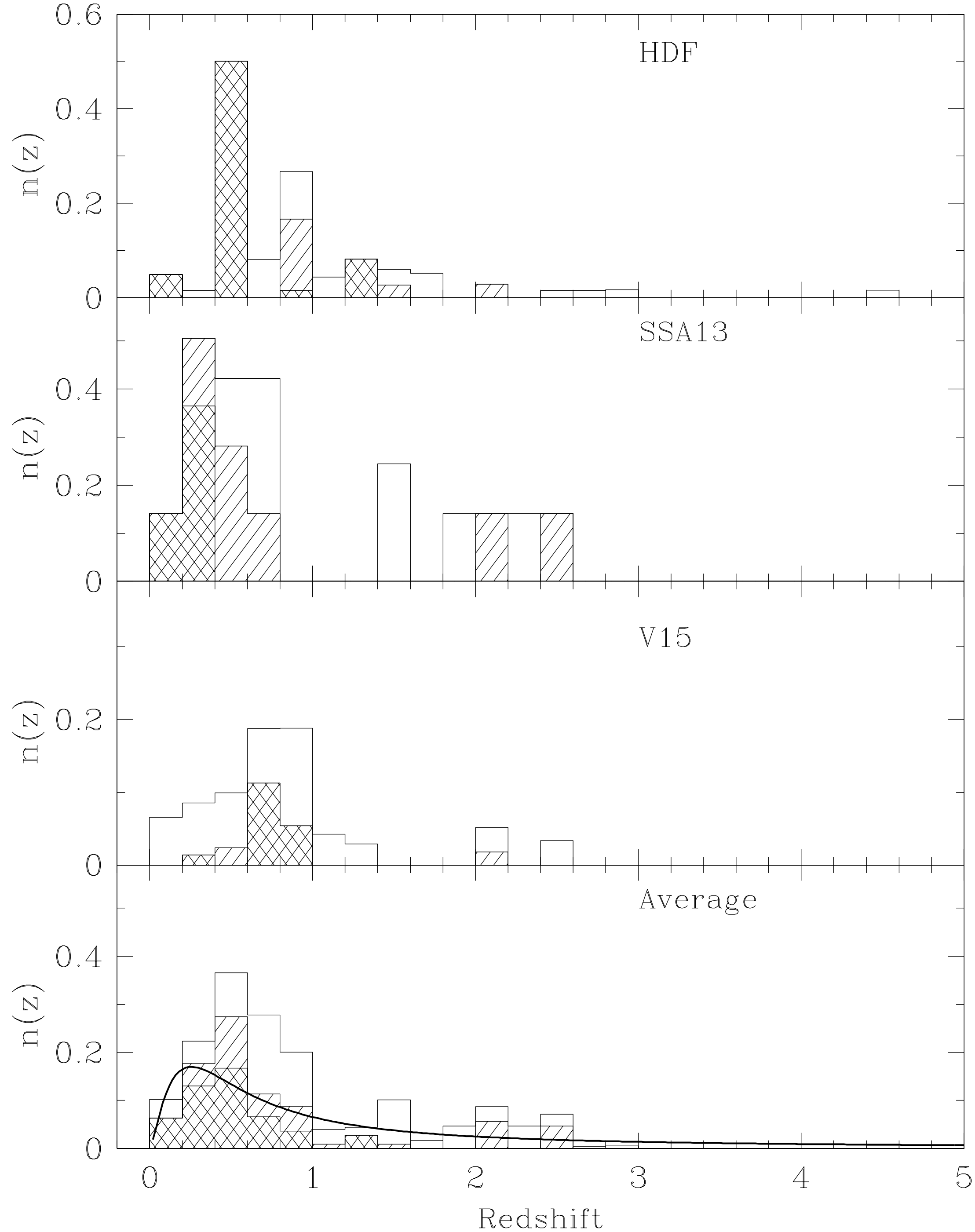

FIG. 5.—Redshift distribution of sources, separated into the " lower " sample (*cross-hash*), " middle " sample (*cross-hash and hash*), and " upper " sample (*all sources shown*). These samples are used in §§ 3 and 4 to calculate a " middle " value with lower and upper limits; see § 2.5 for how samples are defined. The curve is the model prediction based on a fit to the middle sample shown here and other data (see discussion in § 3.3).

fraction of late-type galaxies than originally reported by Hammer et al. (1995); thus, some uncertainty remains. Also, the V15 field lies only 20′ from the cluster associated with 3C 295, and there is another supercluster or redshift structure at $z = 0.98$ within the field (Le Fèvre et al. 1994). These structures have probably caused some bias in the identifications, increasing the fraction of early-type radio galaxies. Thus, we adopt the statistics from the HDF and SSA13 surveys, which imply that about 50% of the sources have disk or late-type galaxy counterparts, 30% have red/optically faint identifications, and 20% are associated with ellipticals and low-luminosity FR I–type AGNs.

2.5. *Strategy for Dealing with Incomplete Identifications and Redshifts*

The goal of this work is to calculate the global star formation history based on star-forming radio sources. Since not all of the sources are star-forming and only 58% have spectroscopic redshifts, we must define the target population carefully. To do this, we separate the data into subsets in order to calculate lower and upper limits on the luminosity function and hence the star formation history (see Fig. 5):

1. A "lower limit" sample (23 sources): only those sources that are both identified with spirals/irregulars/mergers and have spectroscopic redshifts. These are the sources that definitely belong in the population of interest.

2. A "middle value" sample (37 sources): only those sources for which two criteria are met:

a) Redshift is spectroscopic *or* based on *I*- or *HK′*-band magnitude (no randomly assigned redshifts).

b) Galaxy type is spiral/irregular/merger or faint/red. In addition, about 80% of the "unknown" identifications are assumed to be spiral/irregular/merger or faint/red and are included here. The highest redshift source ($z = 4.42$ in the HDF) is not included here because Waddington et al. (1999) argue that it contains an AGN component.

This sample is our best estimate of the true redshift distribution of star-forming radio galaxies.

3. An "upper limit" sample (all 77 sources): all sources (including identifications with elliptical, emission line, and a few Seyfert galaxies, but not verified QSOs, which were removed from the sample). Redshifts were assigned for those sources without spectroscopic or *I*- or *HK′*-band estimates. This sample shows the maximum star formation rate that the data would allow, assuming that all radio flux from all detected sources is due to star formation and that the redshift estimates are correct.

3. EVOLUTION OF THE LUMINOSITY FUNCTION

Next we determine the evolution of the luminosity function for this population of faint star-forming radio galaxies, using the data described in § 2. In § 4.3 we will use this evolving luminosity function to build a model of the star formation history. Since our data contain very few low-redshift objects, we cannot fit for the shape of the local luminosity function. Instead, we use the local luminosity function found by Condon (1989) and fit for the evolution of that function in luminosity and number density. In § 3.1 we calculate the luminosity function directly from the data, in § 3.2 we describe the evolution model, and in § 3.3 we describe the observational constraints on that model and the resulting best fit.

We convert all observed luminosities to a rest-frame frequency of 1.4 GHz, since most of the work on the local luminosity function has been done at this frequency. Our samples are defined at 5 and 8 GHz, but some sources have also been detected at 1.4 GHz. We use the observed 1.4 GHz flux densities when available, and for the remaining sources we assume a spectral index of $\alpha = 0.4$ (see § 1) to convert to 1.4 GHz, unless this violates an observed limit on the 1.4 GHz flux density. All source luminosities are then converted from the observed 1.4 GHz value to their rest-frame 1.4 GHz value. Thus, the observed luminosity of each galaxy $L_{o,\nu}$ at an observing frequency ν and redshift z is converted to the emitted luminosity at 1.4 GHz rest-frame frequency using

$$L_{e,1.4} = L_{o,\nu}\left(\frac{\nu}{1.4\ \mathrm{GHz}}\right)^{\alpha}(1+z)^{\alpha}\ . \qquad (3)$$

We define the luminosity function $\phi(L_{e,1.4})$ as the number per comoving Mpc^3 per $d\log_{10} L$ of star-forming radio sources with emitted luminosity $L_{e,1.4}$(W Hz^{-1}) at 1.4 GHz.

3.1. *Luminosity Function Estimated from the Data*

We can calculate the luminosity function directly from the detected sources for those luminosity and redshift ranges that are sampled by the data sets described in § 2. For each bin in luminosity ($L_{\min} < L_{e,1.4} < L_{\max}$) and redshift ($z_{\min} < z < z_{\max}$), the luminosity function is

$$\phi(L_{e,1.4}, z)d\log_{10} L = \Sigma_i \frac{B_i}{V_c[z_{\min}, z_{\max}(L_i)]}\ , \qquad (4)$$

where B_i is the surface density, corrected for the primary beam (eq. [1]), and $z_{\max}(L_i)$ is the largest z in the bin for which the luminosity of the source L_i was above detection limit of the survey. V_c is the comoving volume (in Mpc^3) between $z_{\min}$ and $z_{\max}$ for solid angle $\Delta\Omega$,

$$\begin{aligned} V_c(z_{\min}, z_{\max}, \Delta\Omega) &= \int d\Omega \int r^2(z)dr \\ &= \frac{\Delta\Omega}{\mathrm{sr}}\left(\frac{\mathrm{sr}}{1.18\times10^7\ \mathrm{arcmin}^2}\right) \\ &\quad\times\frac{[r^3(z_{\max}) - r^3(z_{\min})]}{3}\ , \end{aligned} \qquad (5)$$

where the comoving distance is

$$r(z) = \frac{2c}{H_0}\left(1 - \frac{1}{\sqrt{1+z}}\right) \qquad (6)$$

for our assumed cosmology (see § 1).

The binned luminosity function was calculated using equation (4) for the lower, middle, and upper samples described in § 2.5, using the average of the three surveys (Fig. 5, *bottom panel*). The result is shown in Figure 6, where the data points are from the "middle" sample and are plotted at the average of the luminosities in each bin. Vertical error bars are either the lower and upper limits (from the samples described in § 2.5) or the Poisson errors ($1/N^{1/2}$ weights from the number of galaxies per bin), whichever is larger (generally the Poisson errors dominate for the low-redshift data, and the lower/upper sample limits dominate for the high-redshift data). Horizontal error bars are the range of source luminosities in each bin. Bins were chosen such that each contains four to six galaxies (except for the lowest redshift bin, which has only two galaxies).

3.2. *Description of Evolving Luminosity Function Model*

We now build a model of the evolving luminosity function in order to compare it to several observables. In § 3.3 we describe the observational constraints, the fitting process, and the resulting fit of this model to the observed data. Here we describe the model and its free parameters.

We use the local 1.4 GHz luminosity function for star-forming/spiral galaxies from Condon (1989, eq. [8] and discussion after eq. [7]), adopting different notation,

$$\log_{10}[\phi(L_{e,1.4})]d\log_{10} L = \Big\{28.83 + Y - 1.5\log_{10} L_{e,1.4} - \left[B^2 + \frac{1}{W^2}(\log_{10} L_{e,1.4} - X)^2\right]^{1/2}\Big\}d\log_{10} L\ , \qquad (7)$$

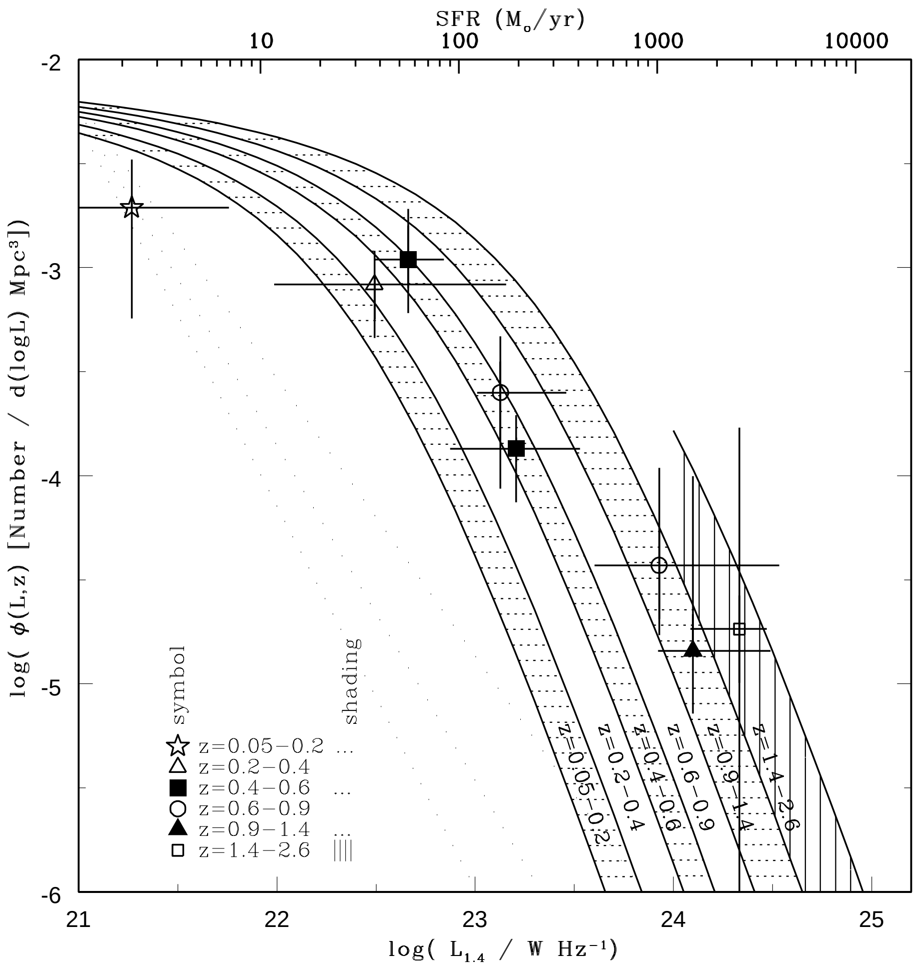

FIG. 6.—Evolving luminosity function for faint star-forming radio sources. Data points are averaged over the three surveys. Symbol shapes and shading correspond to the redshift ranges indicated. Horizontal error bars indicate the range of source luminosities in the bin. Vertical error bars are the larger of the Poisson errors or the lower/upper limits (see § 3.1). The curve is the model evolving luminosity function, found from a fit to these and other data (see discussion in § 3.3).

with the fitted parameters for star-forming galaxies of $Y = 2.88$, $X = 22.40$, $W = \frac{2}{3}$, and $B = 1.5$. The factor of 28.83 includes unit conversions and the conversion from magnitudes ($d \log_{2.5} L$) to base 10 ($d \log_{10} L$).

To describe the evolution of the luminosity function, we use the functional form suggested by Condon (1984b, eq. [24]), a power law in $(1 + z)$ with an exponential cutoff at high redshift. The luminosity evolves as

$$f(z) = (1 + z)^Q \exp\left[-\left(\frac{z}{z_q}\right)^q\right], \qquad (8)$$

and the number density evolves as

$$g(z) = (1 + z)^P \exp\left[-\left(\frac{z}{z_p}\right)^p\right]. \qquad (9)$$

This gives six free parameters (Q, q, z_q, P, p, z_p) to use in describing the evolution. Thus, the general expression for the evolving luminosity function is (Condon 1984a)

$$\phi(L_{e,1.4}, z) = g(z)\,\phi\left[\frac{L_{e,1.4}}{f(z)}, 0\right]. \qquad (10)$$

Once we know the evolving luminosity function, it can be used to predict the observed redshift distribution, $n(z)$. The number of sources between $z_{\rm min}$ and $z_{\rm max}$ that could be detected in a survey of angular area $\Delta\Omega$ and flux limit $S_{\rm lim}$ at frequency ν is

$$n(z) = V_c(z_{\rm min}, z_{\rm max}, \Delta\Omega) \int_{L'(S_{\rm lim}, z)}^{\rm inf} \phi(L_{e,1.4}, z) d \log_{10} L , \qquad (11)$$

where the lower limit of the integral is the luminosity corresponding to the flux limit $S_{\rm lim}$ at the redshift z. The comoving volume V_c is defined in equation (5).

The evolving luminosity function can also be used to predict the extragalactic background due to this population. The background intensity at observing frequency ν_0 is (Dwek et al. 1998)

$$I(\nu_0) = \frac{1}{4\pi} \int \rho(\nu, z) \left|\frac{c\,dt}{dz}\right| dz , \qquad (12)$$

where the luminosity density ρ emitted at redshift z and frequency ν is found from the luminosity function,

$$\rho(\nu, z) = \int L_{e,1.4}\, \phi(L_{e,1.4}, z) d \log_{10} L , \qquad (13)$$

and

$$\left|\frac{dt}{dz}\right| = \frac{1}{H_0(1+z)^{5/2}} \quad (14)$$

for the assumed cosmology (§ 1).

3.3. *Fitting the Evolving Luminosity Function Model to the Data*

We can now compare the evolution model to the observed data in order to fit for the evolution parameters. The model is constrained by three observables:

1. The redshift distribution, $n(z)$. We use the "middle" sample (defined in § 2.5) for the average of three surveys, shown as the hashed area in the bottom panel of Figure 5.
2. The observed luminosity function, shown as the data points in Figure 6. We use the error bars shown in the figure (the larger of lower/upper limits and Poisson errors).
3. The extragalactic radio background, which is an important constraint on the integral of the luminosity function.

The first two constraints are not independent from each other, but both are needed. In order for the observed luminosity function to have four to six sources per bin, only coarse redshift resolution is possible; the $n(z)$ distribution allows for more detailed redshift information but does not include the luminosity information.

The extragalactic radio background is about half due to star formation activity and half due to AGNs (see discussion in Haarsma & Partridge 1998). In order to isolate the part of the radio background due to star formation, we use the far-infrared (FIR) background found by DIRBE of $1.15 \pm 0.20 \times 10^{-20}$ W m^{-2} sr^{-1} Hz^{-1} near 200 μm (Hauser et al. 1998), assumed to be due primarily to star formation. The FIR-radio correlation (Helou, Soifer, & Rowan-Robinson 1985; Condon, Anderson, & Helou 1991) can then be used to predict the portion of the radio background due to star formation, which at 1.4 GHz is $\rho = 3.2 \pm 0.6 \times 10^{-23}$ W m^{-2} sr^{-1} Hz^{-1}.

For each trial set of evolution parameters (Q, q, z_q, P, p, z_p), we calculate the model prediction for $n(z)$, the evolving luminosity function, and the radio background due to star formation. The evolution parameters are adjusted to improve the model fit to the three data constraints, using a downhill simplex algorithm (Press et al. 1992) to find the global χ^2 minimum. Since the $n(z)$ and luminosity function constraints are not independent from each other, the reduced χ^2 cannot be used to calculate the "goodness of fit" or to compare quantitatively the quality of different fits, but its minimum still indicates the parameters of the best available fit.

Our best fit is ($Q = 3.97$, $q = 1.02$, $z_q = 1.39$, $P = -0.0579$, $p = 23.1$, $z_p = 14.3$). The resulting evolution factors $f(z)$ and $g(z)$ are plotted in Figure 7. The $n(z)$ distribution predicted by the model is shown in Figure 5 (*bottom panel*). The peak of the model $n(z)$ distribution falls at a lower redshift ($z \sim 0.3$) than the peak in the data ($z \sim 0.5$), but the tail of the distribution is reasonable and the total number density under the curve is similar (within 5%) for the data and the model (models with a peak at higher redshift tend to have a much shorter tail or a larger total number of sources n and thus a larger discrepancy with the observed total). The luminosity function predicted by the model is shown as the curve in Figure 6 and is a good fit to the data points, except for the $z = 0.05$–0.2 bin (which includes only two galaxies) and the $z = 0.6$–0.9 bin (where one point is too high and the other is too low). The model-predicted star-forming radio background is 3.0×10^{-23} W m^{-2} sr^{-1} Hz^{-1}, which is a reasonable fit to the observed value. While the model does not perfectly match the three data constraints, it is the best compromise between them. Models that give a better fit to the observed $n(z)$ *shape* result in a poor fit to the other two data constraints. For instance, some evolution models can produce a longer tail on the $n(z)$ distribution, but that raises the total background and the total surface density n significantly above the observed levels.

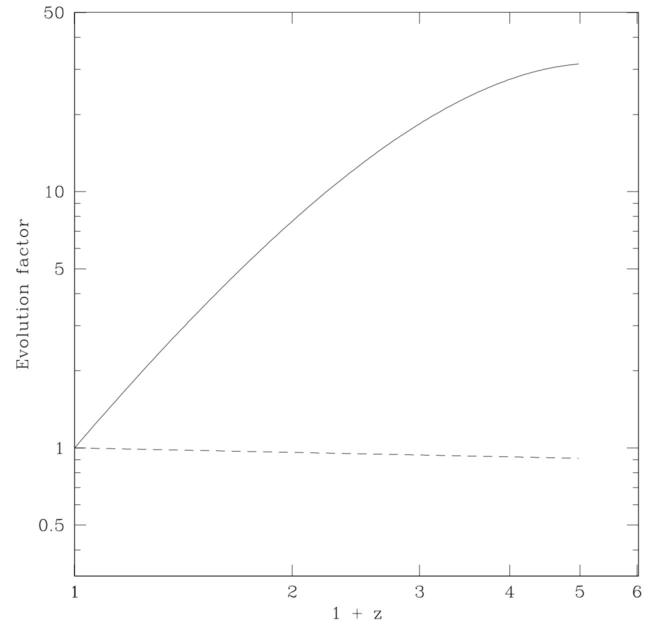

FIG. 7.—Evolution functions for the fitted model found in § 3.3. The solid line is $f(z)$ (luminosity evolution), and the dashed line is $g(z)$ (number density evolution) (see eqs. [8] and [9]).

In the early stages of this work, it seemed that the full six parameters of our evolution model (eqs. [8] and [9]) were necessary to achieve a good fit. In the end, the best-fit model shows virtually no number density evolution and only a mild turnover in luminosity evolution. Pure luminosity evolution [i.e., $f(z) = (1+z)^Q$ and $g(z) = 1$] has often been suggested in the literature (Rowan-Robinson et al. 1993; Hopkins et al. 1998). It turns out that pure luminosity evolution with $Q = 2.74$ gives a similar fit to the luminosity function data points but predicts a tail on the $n(z)$ distribution that extends beyond $z = 5$ and a star-forming radio background that is slightly too high (4.1×10^{-23} W m^{-2} sr^{-1} Hz^{-1}).

The six parameters used here are very interdependent. As we progressed through this work, adding data and model features, we fitted our model to the data numerous times. The resulting fits occurred in a wide range of this parameter space, with the turnover at high redshift sometimes occurring in $f(z)$ (luminosity evolution) and sometimes occurring in $g(z)$ (number density evolution). Some fits had a steeper increase in $f(z)$ and a decrease in $g(z)$, while others had a shallower increase in $f(z)$ and an increase in $g(z)$. This reminds us that the six parameters are degenerate, and most likely a different parameterization with fewer free parameters could describe the data as well. Finding a new parameterization, however, would go beyond the scope of this present work, given the limited sample size currently available. Although the shapes of $f(z)$ and $g(z)$ varied greatly between different fits, all of the fits predicted generally similar shapes for the observables [the $n(z)$ distribution and the luminosity function] and for the predicted global star formation history (see § 4.3).

4. STAR FORMATION HISTORY

Now that we have a model of the evolving luminosity function, we can use it to determine the star formation history. First, we describe the relationship between star formation rate and radio luminosity (§ 4.1), then calculate the star formation history directly from the data with minimal model dependence (§ 4.2), and finally calculate it from the model (§ 4.3).

4.1. *Star Formation Rate from Radio Luminosity*

For an individual star-forming galaxy, the star formation rate (SFR) is directly proportional to its radio luminosity (Condon 1992):

$$\mathrm{SFR} = Q\left\{\frac{L_\nu}{\mathrm{W\ Hz^{-1}}}\Bigg/\left[5.3\times 10^{21}\left(\frac{\nu}{\mathrm{GHz}}\right)^{-0.8} + 5.5\times 10^{20}\left(\frac{\nu}{\mathrm{GHz}}\right)^{-0.1}\right]\right\} M_\odot\ \mathrm{yr^{-1}}\ . \quad (15)$$

Condon (1992) derives this relation by calculating the synchrotron radio emission from supernova remnants (the first term in the denominator) and the thermal radio emission from H II regions (the second term). The spectral index of 0.8 is typical for the nonthermal component of a radio source at 1.4 GHz. This relation is derived purely from radio considerations. Cram et al. (1998), however, compare this relation to Hα studies and find that they give similar star formation rates for local individual galaxies, with the exception of galaxies with extremely large star formation rates. (A. Hopkins et al. 2000, in preparation, have found SFR-dependent dust corrections that shift the optical results to match eq. [15] and radio observations.)

Both the thermal and nonthermal components of the radio expression are proportional to the formation rate of high-mass stars ($M > 5\ M_\odot$), which produce supernovae and large H II regions, so the factor Q is included to account for the mass of all stars in the interval 0.1–100 $M_\odot$,

$$Q = \frac{\int_{0.1\ M_\odot}^{100\ M_\odot} M\psi(M)dM}{\int_{5\ M_\odot}^{100\ M_\odot} M\psi(M)dM}\ , \quad (16)$$

where $\psi(M) \propto M^{-x}$ is the IMF. We have assumed throughout a Salpeter IMF ($x = 2.35$), for which $Q = 5.5$. If an upper limit of 125 $M_\odot$ is used, then $Q = 5.4$. If we use a range of mass 0.25–100 $M_\odot$, as suggested by Gould, Bahcall, & Flynn (1996), then $Q = 3.9$. We will use $Q = 5.5$ in the following.

Condon's relationship (eq. [15]) uses the emitted source luminosity at a frequency of 1.4 GHz, and thus the corrections given in equation (3) must be applied. We should also consider whether there are other ways in which the connection between SFR and radio luminosity might evolve with redshift. At 1.4 GHz, the thermal term in equation (15) is much smaller than the synchrotron term, so evolution in the thermal term will have little effect. In the synchrotron term, the dependence of the emitted flux on the supernova environment is weak (Condon 1992), so little evolution is expected. However, at high redshifts, relativistic electrons may experience significant inverse Compton cooling from the intense FIR energy density or the cosmic microwave background. Another effect that might cause significant evolution in equation (15) is an evolving IMF, entering through the factor Q. In active starbursts, the IMF may be weighted to high-mass stars (Elmegreen 1999), which would result in a smaller value of Q. However, the smallest Q is unity (when virtually all mass occurs in high-mass stars), so the strongest decrease in our calculated star formation history from a radical change in the IMF would be roughly a factor of 5. Note that evolution of the IMF would affect optical estimates of the star formation rate as well. In the following calculations we assume that equation (15) does not evolve.

To determine the star formation rate per comoving volume, we simply substitute the radio luminosity density (such as eq. [13] or eq. [18]) for the source luminosity L_ν in equation (15), giving

$$\Psi(z) = Q\left[\frac{\rho_{e,1.4}(z)}{4.6\times 10^{21}\ \mathrm{W\ Hz^{-1}\ Mpc^{-3}}}\right] M_\odot\ \mathrm{yr^{-1}\ Mpc^{-3}}\ , \quad (17)$$

where 1.4 GHz is used in the denominator of equation (15), as all data have already been converted to 1.4 GHz in the rest frame.

4.2. *Star Formation History Estimated from the Data*

We now calculate the star formation history directly from the survey data in § 2 by using the luminosity density of the detected sources. For each redshift bin ($z_{\min} < z < z_{\max}$), the luminosity density is

$$\rho_{e,1.4}(z) = \Sigma_i \frac{L_i B_i C(z)}{V_c[z_{\min}, z_{\max}(L_i)]}\ , \quad (18)$$

where B_i is the surface density given in equation (1), $C(z)$ is a correction for faint sources described below, $z_{\max}(L_i)$ is the largest z in the bin for which the luminosity of the source L_i was above detection limit of survey, and V_c is the comoving volume given in equation (5). This luminosity density can then be used in equation (17) to find the evolving star formation density. Without the correction factor $C(z)$, the luminosity density includes only individual sources brighter than the flux limit of the survey. It does not include the luminosity density of sources too faint to be detected individually, and so it clearly underestimates the star formation rate [but calculations without $C(z)$ have the advantage of being independent of our evolution model and provide a lower limit].

To account for these faint sources, we use the evolving luminosity function found in § 3.3. Figure 8 illustrates the faint source correction, using a redshift of 1.6 as an example. The integral under the curve in the figure is proportional to the total luminosity density. The flux limit of the survey, however, only allows detection of individual sources above a certain luminosity, i.e., in the cross-hash area. The faint source correction factor $C(z)$ in equation (18) would then be the ratio of the total area to the cross-hash area. We have argued, however, that the slope of the source number counts changes below about 1 μJy (Haarsma & Partridge 1998), so that in fact most of the sources will occupy only the hashed

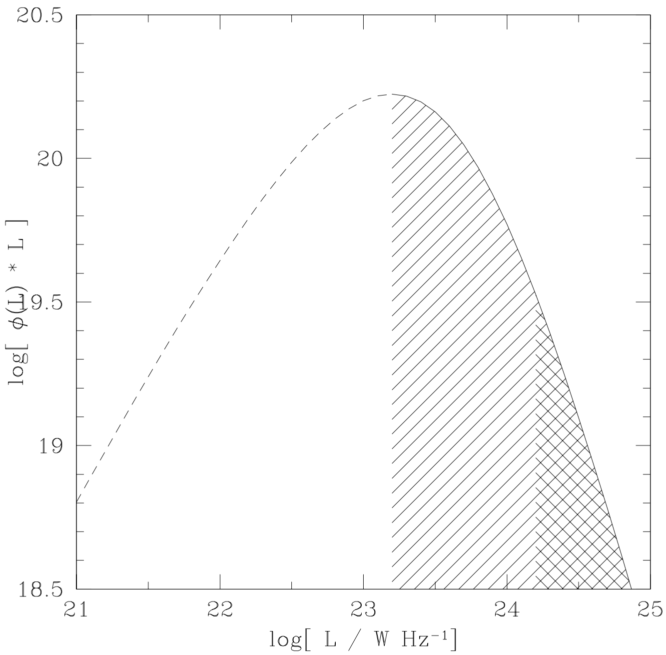

FIG. 8.—Integral under the $\phi(L)L$ curve is proportional to the luminosity density. The relation for redshift $z = 1.6$ is shown. The total luminosity density is due to all sources brighter than $S_{8\,\mathrm{GHz}} \sim 1\ \mu$Jy (*hash*), but only discrete sources above $S_{8\,\mathrm{GHz}} \sim 9\ \mu$Jy are detected in the survey sample (*cross-hash*). The ratio of the two regions gives the correction to the luminosity density needed to account for sources too faint to be detected individually in the survey; here it is about 3.8.

area of Figure 8. Thus, a more realistic correction to equation (18) is the ratio of the hashed region to the cross-hashed region, i.e., the ratio of the luminosity density due to sources brighter than 1 μJy to the luminosity density from sources brighter than the flux limit of the survey,

$$C(z) = \frac{\int_{L(S_{\mathrm{lim}}, z)}^{\mathrm{inf}} L_{e,1.4}\, \phi(L_{e,1.4}, z) d \log_{10} L}{\int_{L(1\ \mu\mathrm{Jy}, z)}^{\mathrm{inf}} L_{e,1.4}\, \phi(L_{e,1.4}, z) d \log_{10} L} . \qquad (19)$$

A list of corrections for several redshifts is given in Table 5. Note that if the slope of the number counts of radio sources were assumed to stay the same below 1 μJy, these corrections would be even larger, and so would the calculated star formation density.

We calculated the star formation density using equations (17), (18), and (19) for the lower, middle, and upper samples described in § 2.5; the results are shown in Figures 9 and 10 and listed in Table 6. Recall that the "lower" sample includes only sources with spectroscopic redshifts and definite identifications with spirals, irregulars, or mergers and thus is the minimum amount of star formation activity consistent with the data. The "middle" value includes some sources with ambiguous identifications and rough photometric redshifts but is our best guess at the total radio-selected star-forming population. The "upper" sample includes all the sources and is the maximum possible star formation activity allowed by the radio data. In Figure 9, the points are values calculated from the middle sample, plotted at the average of the source redshifts in the bin. The vertical error bars are either the limits from the lower and upper samples or the Poisson errors (from the number of galaxies per bin), whichever is larger (in most cases, the lower limits and upper limits are larger than the Poisson errors). To make the lower sample a true lower limit, we did

TABLE 5

FAINT SOURCE CORRECTION FACTORS

REDSHIFT	CORRECTION FACTOR $C(z)$	
	8 GHz, $S_{\mathrm{lim}} = 9\ \mu$Jy	5 GHz, $S_{\mathrm{lim}} = 16\ \mu$Jy
0.28……	1.3	1.5
0.46……	1.6	2.0
0.60……	1.9	2.3
0.81……	2.2	3.0
1.6…….	3.8	5.8

not include the faint source correction $C(z)$. Thus, the lower limit is for only those sources clearly identified with star-forming systems and having spectroscopic redshifts, with no allowance made for evolution of the luminosity function or for sources below the survey flux limits. This is surely a gross underestimate of the true star formation density value, since faint sources, unidentified sources, and sources without spectroscopic redshifts are all missing, but it provides a firm lower limit to the true star formation rate. The "middle" and "upper" samples do have the correction $C(z)$ for faint sources applied.

Mobasher et al. (1999) have done a similar calculation of star formation density from a survey of faint radio sources. They find no evidence for evolution from $z = 0$ to $z = 1$ and a decrease in star formation density above $z = 0.3$. Their

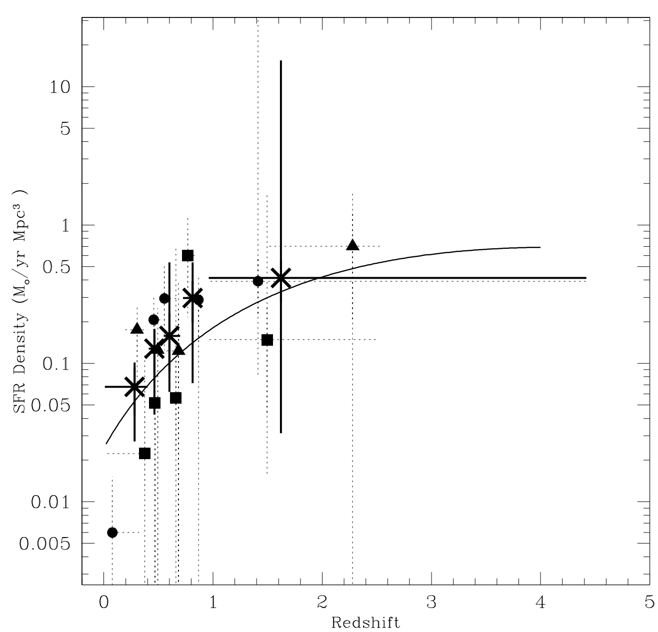

FIG. 9.—Star formation history data points (see § 4.2). Circles are from the HDF field, triangles from the SSA13 field, and squares from the V15 field. The average is shown with crosses and solid error bars. The curve is the star formation history predicted by the model evolving luminosity function (note that this curve was not fitted to the data points shown here; see § 4.3). Vertical error bars are the larger of Poisson errors or lower/upper limits (§ 2.5). Horizontal error bars are the range of source redshifts in the "upper" sample.

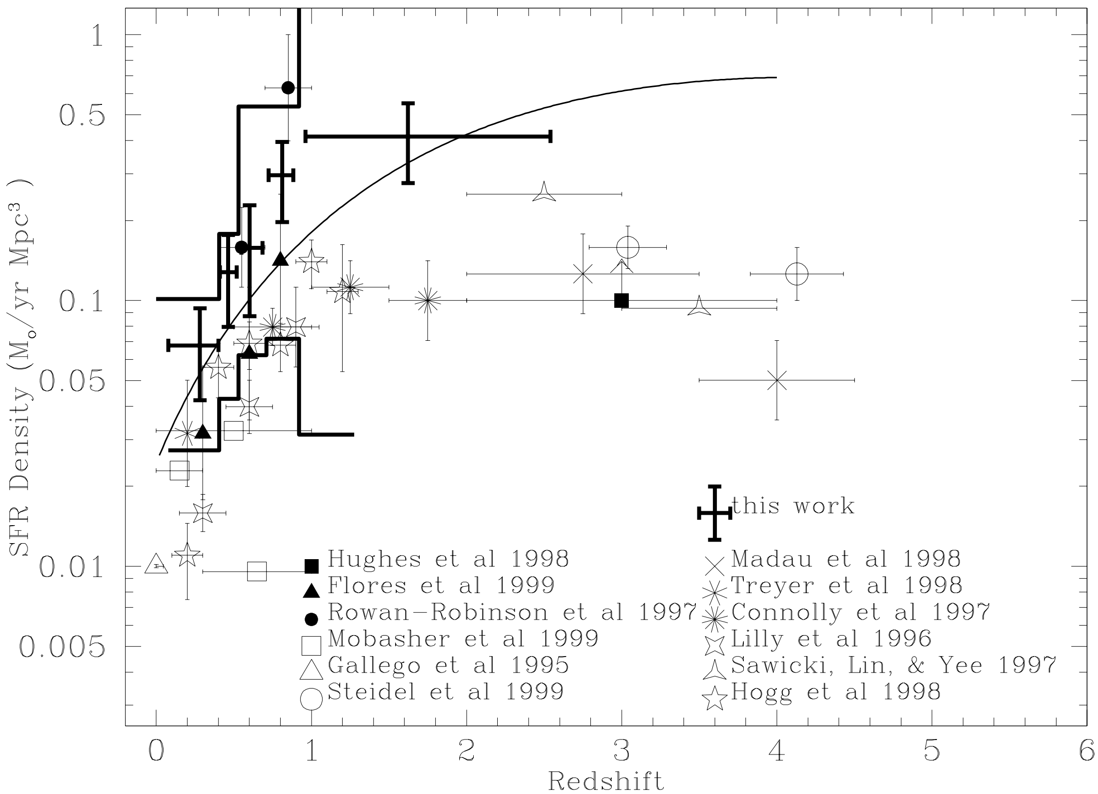

FIG. 10.—Star formation history. Data points are the same as in Fig. 1, with our results overlaid. The thick crosses show the star formation density of our middle sample (defined in § 2.5), with error bars indicating Poisson errors. The thin curve is our model prediction, found in § 4.3 by fitting to the redshift distribution, luminosity function, and extragalactic radio background (not to the thick crosses shown). The thick lines indicate firm lower and upper limits on the star formation density, calculated in § 4.2 using samples defined in § 2.5.

results, however, are based on a radio survey sample that is only 50% complete, and thus their results are highly dependent on assumptions made when correcting for incompleteness. Similarly, their optical identifications and spectroscopic redshifts are much less complete than ours. Finally, the radio surveys we use extend to much fainter flux densities where star formation is more likely to dominate the radio emission. The fainter flux limit also allows us to detect more high-redshift sources. Thus, we believe that our results for the star formation density are more reliable than those of Mobasher et al. (1999).

4.3. *Star Formation History Predicted by Model*

The star formation history can also be determined directly from the evolution model found in § 3.3. We simply calculate the luminosity density emitted at 1.4 GHz (eq. [13]) and use equation (17) to find the star formation density. The resulting star formation density prediction is the curve plotted in Figures 9 and 10.

The model curve in Figures 9 and 10 falls somewhat below the averaged data points (*thick crosses*). Note that the model curve was not fitted to these averaged data points (which were calculated using eqs. [17]–[19]), but rather the model was found from the evolving luminosity function alone (using eqs. [13] and [17]). The evolving luminosity function, in turn, was fitted to the $n(z)$ data, the luminosity function data, and the radio background (see § 3.3). As discussed in § 3.3, our model fits these data well but not perfectly, so small differences between the model prediction and the star formation data points are not unreasonable.

This sort of calculation was previously done by Cram (1998), using the Condon (1989) luminosity function and Condon (1984a) evolution model. Please note the typo-

TABLE 6

STAR FORMATION HISTORY

Redshift		SFR Density ($M_\odot$ yr^{-1} Mpc^{-3})		
Average[a]	Range[b]	Value from Middle Sample	Poisson Error Range	Lower and Upper Limits
0.28	0.010–0.401	0.068	0.042–0.093	0.027–0.101
0.46	0.410–0.518	0.128	0.080–0.176	0.043–0.178
0.60	0.548–0.698	0.158	0.087–0.228	0.062–0.537
0.81	0.724–0.884	0.296	0.197–0.395	0.072–0.536
1.6	0.960–4.42	0.414	0.276–0.552	0.031–15.5

[a] Average redshift in bin from middle sample.
[b] Range of redshifts in bin from upper sample.

graphical error in equation (2) of Cram (1998), which differs by a factor of 28.2 from our equation (15); the correct values were used in their calculations (L. Cram 2000, private communication). We agree with Cram's calculation of 0.026 $M_{\odot}$ yr^{-1} Mpc^{-3} for the local star formation density and calculation of star formation history from Condon's early model.

Note that these methods and results are much improved over our very preliminary work (Haarsma & Partridge 1999), which assumed that the majority of detected faint radio sources lie at the redshift of peak star formation activity. In fact, the peak of the observed redshift distribution (Figs. 3–5) is at a lower redshift than the peak star formation activity (Figs. 9 and 10), as a result of cosmological factors, such as the dependence of the comoving volume on redshift.

5. DISCUSSION AND CONCLUSIONS

Radio wavelength determinations of the universal star formation history have the important advantage of being independent of the dust content of galaxies. Additionally, it is possible to cull relatively clean samples of star-forming objects using radio properties such as spectral index, morphology, and variability. Our results are shown in Figure 10, overlaid with the star formation histories found in several other studies. In Figure 10, the thick crosses show the star formation density of our middle sample, with error bars indicating Poisson errors. Although it is possible that our middle sample may include some low-luminosity AGNs (Seyfert galaxies, etc.), our careful definition of the sample (§ 2.5) and the large fraction of sources with clear optical identifications reduce this contamination. The thin curve is our model prediction, found in § 4.3 by fitting to the luminosity function, redshift distribution, and radio background (not to the thick crosses). The thick lines indicate our lower and upper limits on the star formation density, which are calculated in § 4.2 using samples defined in § 2.5. The lower limit is very firm, since it includes only those sources with spectroscopic redshifts and identifications with spirals, irregulars, and mergers and does not include the star formation in galaxies fainter than the survey detection limit. The upper limit is also firm, since it includes all detected radio sources, even those not associated with star-forming galaxies, but is more uncertain than the lower limit since it includes sources without spectroscopic redshifts.

If we were to assume a different cosmology, our results would change somewhat. The values of H_0, Ω_m, and Ω_Λ affect the calculation of distance from redshift and of luminosity from flux density. The star formation density is proportional to luminosity/volume, so it is inversely proportional to distance and directly proportional to H_0. If we had assumed $H_0 = 100$ km s^{-1} Mpc^{-1} instead of $H_0 =$ 50 km s^{-1} Mpc^{-1}, our data points and model for the star formation density would be twice as large. The values of Ω_m and Ω_Λ also affect the distance measurement. As an extreme example, in a nearly empty but flat universe ($\Omega_m = 0.1$, $\Omega_\Lambda = 0.9$), the distance to a $z = 1$ object is about 1.5 times larger than the distance to it in our assumed cosmology ($\Omega_m = 1, \Omega_\Lambda = 0$), and thus the star formation density would be about $\frac{2}{3}$ of our listed value. Note that all data points in Figures 1 and 10 depend similarly on these cosmological parameters.

At low redshifts, we agree with the findings of many studies that star formation density increases rapidly from the local universe to $z = 1$. We disagree with Cowie, Songaila, & Barger (1999), who find a gradual (rather than steep) increase from $z = 0$ to $z = 1$, and with Mobasher et al. (1999), who find a decrease in star formation density from $z = 0$ to $z = 1$. Our firm lower limit is significantly higher ($z < 1$) than the extinction-corrected optical results of Lilly et al. (1996) at $z \lesssim 0.7$, indicating that some star formation has been obscured by dust. Our "middle sample" data points fall above all the optical and ultraviolet studies shown, indicating that these studies have probably missed some star formation by underestimating the dust extinction (see A. Hopkins et al. 2000, in preparation, for SFR-dependent dust corrections that bring these data more into agreement with our radio results). Our results are similar to the star formation density from the *Infrared Space Observatory* (*ISO*) survey of the HDF (Rowan-Robinson et al. 1997).

At redshifts above $z = 1$, we cannot draw strong conclusions. There are few sources with spectroscopic redshifts in this range, so our calculations are based in large part on less secure photometric redshift estimates and random redshift assignments for the very red objects (§ 2.3). Our assumption that the relationship between radio luminosity and star formation rate does not evolve also becomes less sure as we move to higher redshift (see discussion in § 4.1). The IMF may also be evolving, although this would affect optical and ultraviolet estimates of star formation history as well. Finally, the faint source corrections (eq. [19]; Table 5) become larger at high redshift and thus depend more strongly on the assumed shape of the luminosity function. In fact, at redshifts above 1.5, the current radio survey limits only probe the extreme end of the luminosity function (SFR per galaxy >1000 $M_{\odot}$). Deeper surveys are needed to detect radio counterparts to typical high-redshift optical objects, e.g., Lyman break galaxies (for instance, the predicted radio fluxes for even the most luminous Lyman break galaxies in the HDF are only a few microjanskys at 1.4 GHz; Meurer, Heckman, & Calzetti 1999). Planned improvements to the VLA will allow future surveys to reach this sensitivity.

Still, our calculations at high redshift show that even if a small number of star-forming radio sources exist beyond $z \sim 1.5$, they would indicate a large, optically hidden fraction of star formation density. In particular, the population of radio sources with faint, red optical counterparts may be dust-enshrouded (Richards et al. 1999; Barger et al. 2000; Waddington et al. 1999, § 2.4) and hence missed even in the deepest optical and ultraviolet studies. Deeper high-resolution radio observations, accompanied by close to complete spectroscopic identifications, are needed to determine accurately the amount of "hidden" star formation in the early universe.

D. B. H. and R. B. P. acknowledge the support of NSF grant AST 96-16971 and the Keck Northeast Astronomy Consortium. D. B. H. acknowledges the support of a Cottrell College Science Award from Research Corporation. E. A. R. acknowledges support from Hubble Fellowship grant HG-0123.01-99A and from STScI, which is operated by AURA under NASA contract NAS 5-26555. R. A. W. acknowledges support from AST 88-21016 and AST 98-02963 from the National Science Foundation and NASA grants AR-6948.04-96A and GO-7452.01-96A from STScI under NASA contract NAS5-26555. We are grateful to James Lowenthal for providing us with spectroscopic redshifts in advance of publication. We thank Ian Waddington, Ed Fomalont, Ken Kellermann, and Andrew Hopkins for helpful comments and discussions and our anonymous referee for detailed and helpful comments on the manuscript.

REFERENCES

Barger, A. J., Cowie, L. L., & Richards, E. A. 2000, AJ, 119, 2092
Barger, A. J., Cowie, L. L., Trentham, N., Fulton, E., Hu, E. M., Songalia, A., & Hall, D. 1999, AJ, 117, 102
Baugh, C. M., Cole, S., Frenk, C. S., & Lacey, C. G. 1998, ApJ, 498, 504
Benn, C. R., Rowan-Robinson, M., McMahon, R. G., Broadhurst, T. J., & Lawrence, A. 1993, MNRAS, 263, 98
Brinchmann, J., et al. 1998, ApJ, 499, 112
Bruzual, A. G., & Charlot, S. 1993, ApJ, 405, 538
Cohen, J. G., Cowie, L. L., Hogg, D. W., Songaila, A., Blandford, R., Hu, E. M., & Shopbell, P. 1996, ApJ, 471, L5
Cohen, J., Hogg, D., Blandford, R., Cowie, L., Hu, E., Songaila, A., Shopbell, P., & Richberg, K. 2000, ApJ, 538, 29
Condon, J. J. 1984a, ApJ, 287, 461
———. 1984b, ApJ, 284, 44
———. 1989, ApJ, 338, 13
———. 1992, ARA&A, 30, 575
Condon, J. J., Anderson, M. L., & Helou, G. 1991, ApJ, 376, 95
Connolly, A. J., Szalay, A. S., Dickinson, M., SubbaRao, M. U., & Brunner, R. J. 1997, ApJ, 486, L11
Cowie, L. L., Songaila, A., & Barger, A. J. 1999, AJ, 118, 603
Cowie, L. L., Songaila, A., Hu, E. M., & Cohen, J. G. 1996, AJ, 112, 839
Cram, L. 1998, ApJ, 506, L85
Cram, L., Hopkins, A., Mobasher, B., & Rowan-Robinson, M. 1998, ApJ, 507, 155
Downes, D., et al. 1999, A&A, 347, 809
Dwek, E., et al. 1998, ApJ, 508, 106
Elmegreen, B. G. 1999, ApJ, 515, 323
Flores, H., et al. 1999, ApJ, 517, 148
Fomalont, E. B., Kellermann, K. I., Windhorst, R. A., & Kristian, J. A. 1991, AJ, 102, 1258
Gallego, J., Zamorano, J., Aragón-Salamanca, A., & Rego, M. 1995, ApJ, 455, L1
Gould, A., Bahcall, J. N., & Flynn, C. 1996, ApJ, 465, 759
Gruppioni, C., Mignoli, M., & Zamorani, G. 1999, MNRAS, 304, 199
Haarsma, D. B., & Partridge, R. B. 1998, ApJ, 503, L5
———. 1999, in 9th Astrophys. Conf., After the Dark Ages: When Galaxies Were Young, ed. S. S. Holt & E. P. Smith (New York: AIP), 345
Hammer, F. 1996, in Science with the *Hubble Space Telescope* II, ed. P. Benvenuiti, F. D. Machetto, & E. J. Schreier (Baltimore: STScI), 101
Hammer, F., Crampton, D., Lilly, S. J., Le Fèvre, O., & Kenet, T. 1995, MNRAS, 276, 1085
Hauser, M. G., et al. 1998, ApJ, 508, 25
Helou, G., Soifer, B. T., & Rowan-Robinson, M. 1985, ApJ, 298, L7
Hogg, D. W., Cohen, J. G., Blandford, R., & Pahre, M. A. 1998, ApJ, 504, 622
Hopkins, A., Afonso, J., Cram, L., & Mobasher, B. 1999, ApJ, 519, L59
Hopkins, A. M., Mobasher, B., Cram, L., & Rowan-Robinson, M. 1998, MNRAS, 296, 839
Hughes, D., et al. 1998, Nature, 394, 241
Le Fèvre, O., Crampton, D., Hammer, F., Lilly, S. J., & Tresse, L. 1994, ApJ, 423, L89
Lilly, S. J., Eales, S. A., Gear, W. K. P., Hammer, F., Le Fèvre, O., Crampton, D., Bond, J. R., & Dunne, L. 1999, ApJ, 418, 641
Lilly, S. J., Le Fèvre, O., Hammer, F., & Crampton, D. 1996, ApJ, 460, L1
Lowenthal, J. D., et al. 1997, ApJ, 481, 673
Madau, P., Ferguson, H. C., Dickinson, M. E., Giavalisco, M., Steidel, C. C., & Fruchter, A. 1996, MNRAS, 283, 1388
Madau, P., Pozzetti, L., & Dickinson, M. 1998, ApJ, 498, 106
Meurer, G. R., Heckman, T. M., & Calzetti, D. 1999, ApJ, 521, 64
Mobasher, B., Cram, L., Georgakakis, A., & Hopkins, A. 1999, MNRAS, 308, 45
Oort, M. J. A., & Windhorst, R. A. 1985, A&A, 145, 405
Pascarelle, S. M., Lanzetta, K. M., & Fernández-Soto, A. 1998, ApJ, 508, L1
Press, W. H., Flannery, B. P., Teukolsky, S. A., & Vetterling, W. T. 1992, Numerical Recipes (2d ed.; Cambridge: Cambridge Univ. Press)
Richards, E. A. 1999, ApJ, 513, L9
———. 2000, ApJ, 533, 611
Richards, E. A., Fomalont, E. B., Kellermann, K. I., Windhorst, R. A., Partridge, R. B., Cowie, L. L., & Barger, A. J. 1999, ApJ, 526, L73
Richards, E. A., Kellermann, K. I., Fomalont, E. B., Windhorst, R. A., & Partridge, R. B. 1998, AJ, 116, 1039
Rowan-Robinson, M., Benn, C. R., Lawrence, A., McMahon, R. G., & Broadhurst, T. J. 1993, MNRAS, 263, 123
Rowan-Robinson, M., et al. 1997, MNRAS, 289, 490
Sawicki, M. J., Lin, H., & Yee, H. K. C. 1997, AJ, 113, 1
Steidel, C. C., Adelberger, K. L., Gavalisco, M., Dickinson, M., & Pettini, M. 1999, ApJ, 519, 1
Treyer, M. A., Ellis, R. S., Milliard, B., Donas, J., & Bridges, T. J. 1998, MNRAS, 300, 303
Waddington, I., Windhorst, R. A., Cohen, S. H., Partridge, R. B., Spinrad, H., & Stern, D. 1999, ApJ, 526, L77
Windhorst, R. A., et al. 1994a, AJ, 107, 930
Windhorst, R. A., Fomalont, E. B., Kellermann, K. I., Partridge, R. B., Richards, E., Franklin, B. E., Pascarelle, S. M., & Griffiths, R. E. 1995, Nature, 375, 471
Windhorst, R. A., Fomalont, E. B., Partridge, R. B., & Lowenthal, J. D. 1993, ApJ, 405, 498
Windhorst, R. A., Gordon, J. M., Pascarelle, S. M., Schmidtke, P. C., Keel, W. C., Burkey, J. M., & Dunlop, J. S. 1994b, ApJ, 435, 577